Brandon Ludwig

Mechanical and Aerospace Engineering, Missouri University of Science and Technology, 400 West 13th Street, Rolla, MO 65409

Jin Liu

Mechanical Engineering, Worchester Polytechnic Institute, 100 Institute Road, Worchester, MA 01609

Yangtao Liu

Mechanical Engineering, Worchester Polytechnic Institute, 100 Institute Road, Worchester, MA 01609

Zhangfeng Zheng

Mechanical Engineering, Worchester Polytechnic Institute, 100 Institute Road, Worchester, MA 01609

Yan Wang

Mechanical Engineering, Worchester Polytechnic Institute, 100 Institute Road, Worchester, MA 01609

Heng Pan¹

Mechanical and Aerospace Engineering, Missouri University of Science and Technology, 400 West 13th Street, Rolla, MO 65409 e-mail: hp5c7@mst.edu

Simulation of Micro/Nanopowder Mixing Characteristics for Dry Spray Additive Manufacturing of Li-Ion Battery Electrodes

A new dry spraying additive manufacturing method for Li-ion batteries has been developed to replace the conventional slurry-casting technique for manufacturing Li-ion battery electrodes. A dry spray manufacturing process can allow for the elimination of the time- and energy-intensive slurry drying process needed due to the use solvents to make the electrodes. Previous studies into the new manufacturing method have shown successful fabrication of electrodes which have strong electrochemical and mechanical performance. Li-ion battery electrodes typically consist of three basic materials: active material (AM), binder particle additives (BPA), and conductive particle additives (CPA). In this paper, a discrete element method (DEM) simulation was developed and used to study the mixing characteristics of dry electrode powder materials. Due to the size of the particles being in the submicron to micron size range, the mixing characteristics are heavily dependent on van der Waals adhesive forces between the particles. Therefore, the effect the Li-ion battery electrode material surface energy has on the mixing characteristics was studied. Contour plots based on the DEM simulation results where the surface energy components of selected material types are changed were used to predict the mixing characteristics of different particle systems. For the cases studied, it is found that experimental mixing results are representative of the results of the DEM simulations. [DOI: 10.1115/1.4037769]

1 Introduction

Li-ion battery electrodes consist of four basic components: two electrodes (cathode and anode), a separator, and an electrolyte. The electrode components are made with three essential materials: the active material (AM), binder particle additive (BPA), and conductive particle additive (CPA). The AM is needed to provide the energy for the battery while the CPA is dispersed among the AM to improve the electroconductivity of the electrode. Binder particle additives are needed to secure the electrode material to the current collecting substrate (typically aluminum for the cathode and copper for the anode). Commercial Li-ion battery electrodes are manufactured using the slurry-casting technique. In this manufacturing method, the electrode materials are mixed with a solvent to dissolve the BPA. This allows the BPA to readily coat the remaining particles (AM and CPA). The binder, most commonly polyvinylidene fluoride (PVDF), is matched with a suitable solvent, most commonly N-methyl-2-pyrrolidone (NMP), to allow for optimal mixing and coating.

Due to the direct influence of CPA and BPA distribution on the electrochemical properties, extensive mixing studies have been performed to understand the slurry preparation process on the electrode morphology [1,2]. The effect of multiple mixing steps

and the length of mixing (some up to 48 h) have been studied [3]. Once mixed, the slurry is cast onto the current collector and must be dried to create a dry porous electrode for further battery fabrication. The drying process can take a significant amount of time and energy (up to 24 h at 80-120 °C), which increases the manufacturing cost of the battery electrodes [4,5]. In commercial applications, an expensive NMP recovery system is used to recover evaporated NMP due to the environmentally hazardous properties of NMP [6-10]. More environmentally friendly solvents, such as aqueous based slurries, can be used to eliminate the need for a recovery system but the differences in slurry rheology need to be accounted for [10-12]. The use of aqueous based slurry necessitates the change to a matching binder, such as carboxymethyl cellulose [6,9,11,13], as PVDF needs nonaqueous solvent to sufficiently dissolve [1]. The slurry mixing properties must be accounted for as high surface tension due to strong hydrogen bonding can cause particles to agglomerate and electrode cracking problems can occur during the drying step [10,14,15].

Eliminating the solvent, and its associated drying process, represents an ideal manufacturing process. Working electrodes have been successfully manufactured using pulsed laser and sputtering deposition but are handicapped by slow deposition rates and high annealing temperatures, making commercial feasibility difficult [16–20]. A new electrode manufacturing method using dry electrostatic spraying [21,22] shows a promising alternative to the commercial slurry-casting technique due to its strong performance and capability of reducing costs by \sim 15%. The new method requires only enough time for the BPA to melt to ensure strong

Journal of Micro- and Nano-Manufacturing Copyright © 2017 by ASME

DECEMBER 2017, Vol. 5 / 040902-1

¹Corresponding author.

Contributed by the Manufacturing Engineering Division of ASME for publication in the JOURNAL OF MICRO- AND NANO-MANUFACTURING. Manuscript received June 15, 2017; final manuscript received August 21, 2017; published online September 27, 2017. Assoc. Editor: Yayue Pan.

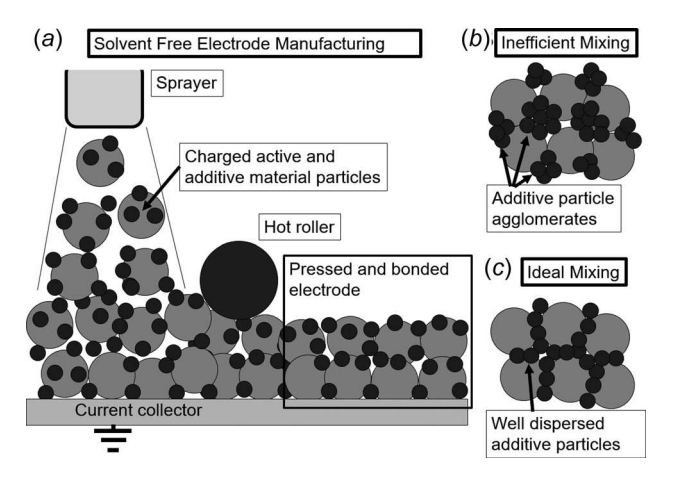


Fig. 1 Solvent-free manufacturing process: (a) schematic of dry electrostatic spraying system, (b) representation of poorly mixed Li-ion battery electrode powders with agglomerations of additive particles, and (c) representation of well mixed Li-ion battery electrode powders with uniform distribution of additive particles

mechanical properties [21] as opposed to the time associated with drying out the solvent in the conventional process. Figure 1(a)shows a diagram of the new manufacturing process using dry electrostatic spraying. Unlike slurry-cast electrodes, the BPA is not dissolved in solvent and coated on the remaining particles, and therefore, a uniform distribution of the BPA within the AM and CPA is needed to ensure strong mechanical bonding. Cases of BPA and CPA agglomeration (Fig. 1(b)) could lead to weak points allowing for poor electroconductivity and mechanically weak locations. Uniform mixing of the additive materials will display minimal agglomerates (Fig. 1(c)) leading to more efficient use of the additive materials. Previous studies [21,22] show that the electrodes fabricated using the new solvent-free process are stronger than those of the conventional method while also displaying similar electrochemical performance to that of the conventional process. While this new method has produced electrodes with strong electrode performance, the mixing properties of dry battery electrode materials is not well known.

In this paper, the mixing characteristics of dry electrode powders used in the new dry manufacturing process will be studied. Previous studies pertaining to mixing the electrode materials used in the slurry-cast technique are not relevant to the new manufacturing technique, and thus, this paper focuses on understanding the dry powder mixing process to help predict BPA and CPA distribution within a given AM. To study the mixing behavior of Lion battery electrode materials, a discrete element method (DEM) simulation has been developed to understand the effect material properties have on the mixing uniformity of Li-ion battery electrode particles. The developed DEM simulation is based on a soft-

sphere model where it is assumed the colliding particles will form small deformations upon impact. The resulting deformation will cause a contact area between the two particles, which is then subject to adhesive forces. Due to the micron and submicron size of Li-ion battery electrode materials, the particle mixing is strongly dependent on adhesive interactions once the particles collide [23,24]. The DEM simulation results can then be used for future studies and Li-ion battery electrode materials to better estimate the mixing properties.

2 Discrete Element Simulation Modeling

To understand the mixing of micro/nanosized powders which represent the AM, BPA, and CPA powders, a DEM model for adhesive fine particles has been developed. Due to the particle sizes being in the nanometer to micrometer size range, the proposed simulation model is heavily dependent on the surface adhesive force interactions between the particles [23,24]. This adhesive force is related to the interfacial energies of the Li-ion electrode materials.

Motion of the individual particles can be described by Newton's second law of motion, and the governing equation for the translational motion of the particles can be defined by

$$m_i \frac{d^2 \vec{r}_i}{dt^2} = \vec{F}_i^{\text{adh}} + \vec{F}_i^{\text{grav}} \tag{1}$$

where m_i and r_i are the mass and position vector of a particle i, respectively. F^{adh} and F^{grav} represent the adhesive contact forces due to particle collisions and gravitational forces, respectively.

Since van der Waals adhesive forces act in a nonlinear fashion with the other forces acting on particles, such as sliding resistance and elastic repulsion, they cannot be simply added to them [23]. The sum of the adhesive and collision forces, $F^{\rm adh}$, on a particle is given by

$$\vec{F}_i^{\text{adh}} = F_n \vec{n} \tag{2}$$

where n is the unit normal along the line passing through the particle centroids; F_n and F_s are the normal force and sliding force magnitude, respectively; and F_n is composed of the elastic term $F_{\rm ne}$ and the damping term $F_{\rm nd}$.

For this study, only the normal force is considered. In order to calculate normal force, contact area between two particles is modeled based on a soft-sphere model where two separate particles will experience deformation upon collision, forming a contact area (Fig. 2(a)). Chokshi et al. [25] modified the contact theory proposed by Johnson, Kendall, and Roberts [26] to simplify the contact radius, a_0 , to

$$a_0 = \left(\frac{9\pi w_{ij}R^2}{2E}\right)^{1/3} \tag{3}$$

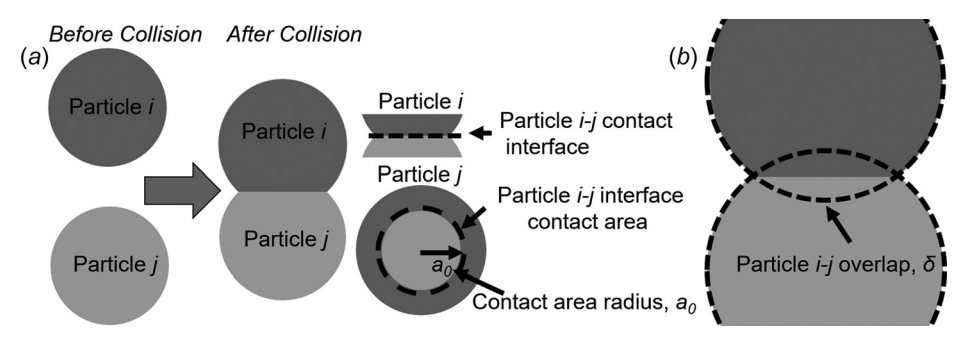


Fig. 2 Contact mechanics of colliding particles: (a) contact interface and radius representation due to the collision of i and j particles and (b) representation of the i-j particle overlap due to collision

040902-2 / Vol. 5, DECEMBER 2017

Transactions of the ASME

where R and E are the effective particle radius and elastic moduli, respectively. Here, R and E are defined as

$$\frac{1}{R} = \frac{1}{R_i} + \frac{1}{R_i} \tag{4}$$

$$\frac{1}{E} = \frac{1 - v_i^2}{E_i} + \frac{1 - v_j^2}{E_i} \tag{5}$$

where two particles are considered with radii R_i and R_j , elastic moduli E_i and E_j , Poisson's ratios v_i and v_j . Table 1 shows the material property values needed for the DEM simulations. The work of adhesion, w_{ij} , between the two particles can be defined by using the Fowkes equation [27]

$$w_{ij} = 2(\gamma_i^d \gamma_i^d)^{0.5} + 2(\gamma_i^p \gamma_i^p)^{0.5}$$
(6)

where γ_i^d and γ_j^d are the dispersive surface energy component values for material i and j, respectively, and γ_i^P and γ_j^P are the polar surface energy component values for material i and j, respectively. The contact area at the work of adhesion interface can be defined as $A_{ii} = \pi a_0^2$.

Chokshi et al. [25] proposed that the normal force, F_{ne} , could be rearranged in terms of the contact radius to

$$F_{\text{ne}} = F_C \left[4 \left(\frac{a}{a_0} \right)^3 - 4 \left(\frac{a}{a_0} \right)^{3/2} \right] \tag{7}$$

where F_C is the critical force given by $F_C = 3\pi w_{ij}R/2$ and a/a_0 can be found by solving

$$\delta_N = 6^{1/3} \delta_C \left[2 \left(\frac{a}{a_0} \right)^2 - \frac{4}{3} \left(\frac{a}{a_0} \right)^{1/2} \right] \tag{8}$$

where δ_N is the normal particle overlap defined in Eq. (9) and δ_C is the particle overlap when at the critical force F_C . When a separation force is applied and the spheres begin to stretch, forming a neck between the two spheres, the critical particle overlap δ_C is equal to δ_N when separation finally occurs. In relation to the equilibrium radius a_0 , the critical particle overlap δ_C is given by Eq. (10)

$$\delta_N = R_i + R_i - |x_i - x_i| \tag{9}$$

$$\delta_C = \frac{a_0^2}{2(6)^{1/3}R} \tag{10}$$

where x_i and x_j denote the centroid positions of the two particles. In this case, the normal particle overlap δ_N does not actually overlap but represent the amount of overlap that would occur if the spheres had not deformed and flattened (Fig. 2(*b*)).

A damping normal force $F_{\rm nd}$ makes up the second part of the normal force F_n and is defined as

$$F_{nd} = -\eta_N \vec{v}_r \cdot \vec{n} \tag{11}$$

where the η_N is the normal dissipation coefficient (chosen to be 0.05 for this study) and ν_R is the relative particle velocity. The normal dissipation coefficient η_N is assumed to have the form

$$\eta_N = \alpha (mk_N)^{1/2} \tag{12}$$

where α is a function of the restitution coefficient (chosen to be 1) [28]. The normal stiffness coefficient, k_n , is estimated by F_n/δ_N .

Software used for performing the DEM simulations was developed from in-house code. The size of the mixing volume was set such that the particles can interact with one another without being limited by space. The boundary conditions were set to simulate a mixing container and therefore the walls were set to be reflective. One hour of computation time yields $\sim 12 \, \mu s$ of mixing time in cases involving a larger number of particles (~ 200) but lower particle numbers will allow for more mixing time.

3 Results

The DEM results can be used to study the surface energy effects on mixing for any particulate system, but for this study the effect of battery electrode materials was considered. Different mixing cases were considered to show how AM surface energy affects the BPA distribution and also how CPA surface energy component values affect the distribution of CPA when mixed with AMs with different surface energy values. The mixing behavior of BPAs and CPAs was also considered as the mixing morphology of these materials directly influences the electrode mechanical strength and electroconductivity. Finally, the mixing behavior of all three material types is characterized.

3.1 Active Material-Binder Particle Additive. Due to Liion battery AM displaying various surface energy component values, the effect of the AM surface energy components on the BPA distribution was studied. From previous studies [12,22], the dispersive component for cathode AM can range from 37.0 to 42.5 mN m⁻¹ while the polar components could be from 1.35 to 177 mN m⁻¹. This extreme range of polar components could lead to a vast difference in mixing uniformity of the BPA within the AM. A DEM simulation consisting of a single 10 μ m particle, acting as the AM particle, and thirty $0.5 \mu m$ particles, acting as the BPA particles, was used to characterize the AM-BPA mixing. Surface energy components of the BPA were set according to previously measured PVDF values (dispersive and polar surface energy components were calculated to be 24.33 mN m⁻¹ and 6.18 mN m⁻¹, respectively [21]) as PVDF is a common BPA in Li-ion battery electrodes. The PVDF surface energy values are also consistent with previous studies [29,30] where PVDF surface energy is measured. The BPA particles were set to be monosized due to experimental studies using PVDF particles show a particle standard deviation within 8% of the average. The BPA underwent a premixing process to form an agglomerate of BPA (Fig. 3(a)). After premixing, the BPA agglomerate is allowed to interact with the AM particle. In the case of aggregation, it is expected that the BPA agglomerate will experience minimal changes after interacting with the AM particle (Fig. 3(b)). In the case of intermixing, it is expected that the BPA agglomerate will begin to break apart and attach to the AM particle, forming a layer (Fig. 3(c)). In the DEM simulations, the output can be used to count the number of BPA in contact with the AM particle.

A contour plot (Fig. 3(d)) of the contact points over a range of surface energy components shows that low dispersive energy values (0–10 mN m⁻¹) and polar energy values from 0 to 35 mN m⁻¹ of active material results in the BPA agglomerate experiencing minimal break-up when interacting with the active material

Table 1 Material input parameters for DEM simulations

Material	Radius, R (μm)	Density, ρ (g cm ⁻³)	Young's modulus, E (GPa)	Poisson's ratio (v)
AM	5	4.90	38	0.18
BPA	0.25	1.78	4.3	0.34
CPA	0.125	2.20	5.0	0.23

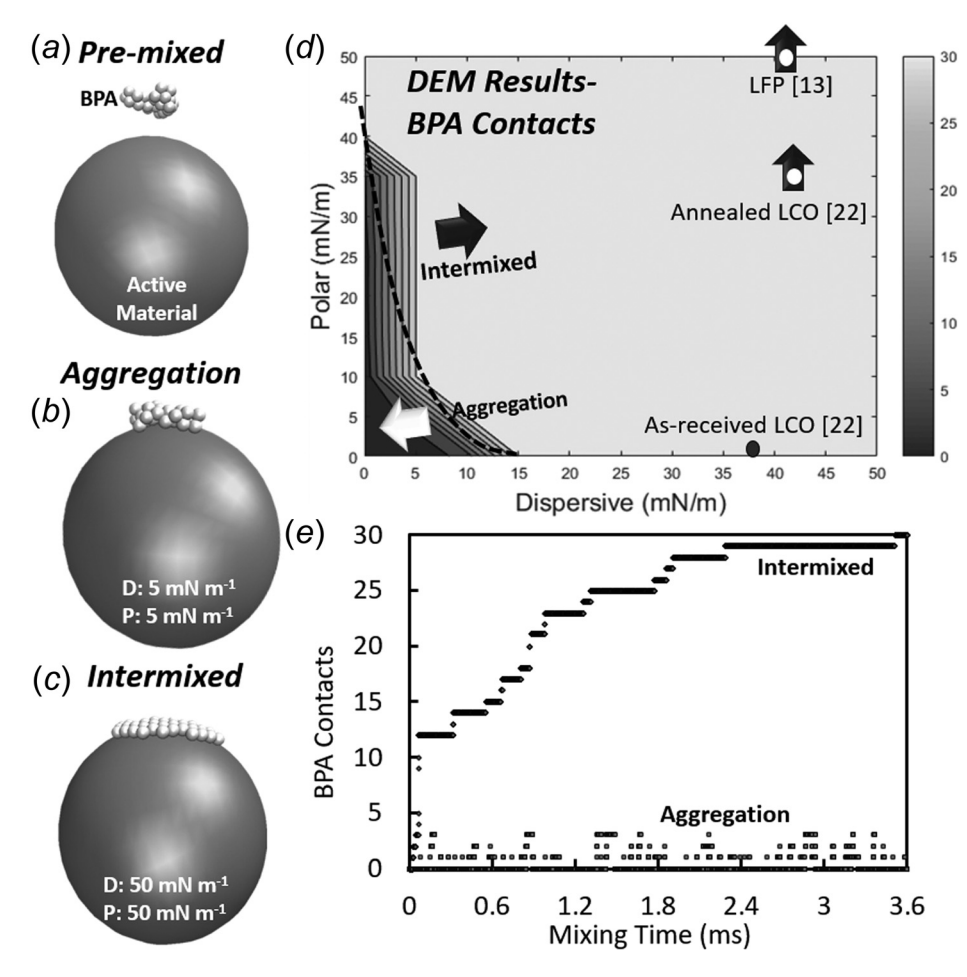


Fig. 3 AM-BPA mixing. DEM simulation snapshots of AM-BPA mixing showing (a) premixing, (b) aggregation, and (c) intermixing. Analytical (d) and DEM (e) contour plots showing similar mixing behavior. (f) Comparison of mixing time found in DEM cases where intermixing and aggregation occurs.

particle (Fig. 3(b) shows a DEM simulation result where aggregation was found). In this range, the BPA agglomerate would either weakly attach to the AM particle surface or bounce on and off of the AM particle due to very weak work of adhesion between the AM-BPA surfaces. Outside of the range, the DEM simulation results show BPA beginning to form a monolayer on the AM surface (Fig. 3(c) shows a DEM simulation result where intermixing was found). For both cases, intermixed and aggregation, the mixing time and the evolution of the contact points can be compared in Fig. 3(e). In the intermixed case, the time to achieve all BPA contacts on the AM particle was \sim 2.4 ms. It can be seen that the number of contacts in the intermixed case gradually increased while the aggregation case exhibited sporadic BPA contact with the AM particle, further showing the weak attraction between the two materials. Known AM surface energy components were added to the DEM contour plot results to show how BPA is expected to mix with the AM (Fig. 3(d)).

3.2 Active Material-Conductive Particle Additive. In this case, the surface energy components of the CPA were allowed to vary while the dispersive and polar surface energy components of the AM particle were kept constant at 40 mN m⁻¹ and 2 mN m⁻¹, respectively. The surface energy component values for the AM were selected to represent a case where negligible polar surface energy component is experienced as is the case of the previously measured as-received LiCoO₂ (LCO) [22]. Similar to the AM-BPA case, the AM-CPA DEM simulations involved a single

 $10 \,\mu \text{m}$ AM particle while the CPA were represented by $0.25 \,\mu \text{m}$ particles (200 in total). The particles representing CPA were set to be monosized due to experimental measurements using Super C65 carbon showing a standard deviation of \sim 11% of the average size. Initially, a premixing step was incorporated into the DEM simulations to form an agglomerate of CPA (Fig. 4(a)). For intermixing to occur, the CPA should begin to assemble on the AM surface (Fig. 4(b)) while minimal CPA assembly should happen when aggregation occurs (Fig. 4(c)). A series of DEM simulations were used to plot the number of CPA contacts on the AM surface (Fig. 4(d)). The DEM contour plots show that the location of peak intermixing is at 20 mN m⁻¹ dispersive component and 0 mN m⁻¹ polar component. Figure 4(b) shows the DEM mixing results from a simulation using 20 mN m⁻¹ dispersive energy and 0 mN m⁻¹ energy and it can be seen that the CPA agglomerate has broken apart and formed on the surface of the AM particle. In the contour plot (Fig. 4(d)), the intermixing to aggregation trend is found to radiate from the peak intermixing location. The crossover location denoting a change between intermixing and aggregation is near the 25-50 contact point area location in the DEM contour plot. This area in the DEM contour plot shows the location where the CPA agglomerate attaches to the AM particle and slowly begins to form around the AM surface. The 0-25 contact point area in the DEM results denotes where very few CPA are in contact with the AM particle (Fig. 4(c)). In this case, the CPA comes into contact with the AM but does not alter its shape to conform to the AM surface.

Active material-conductive particle additive mixing behavior was further studied by increasing the polar surface energy

040902-4 / Vol. 5, DECEMBER 2017

Transactions of the ASME

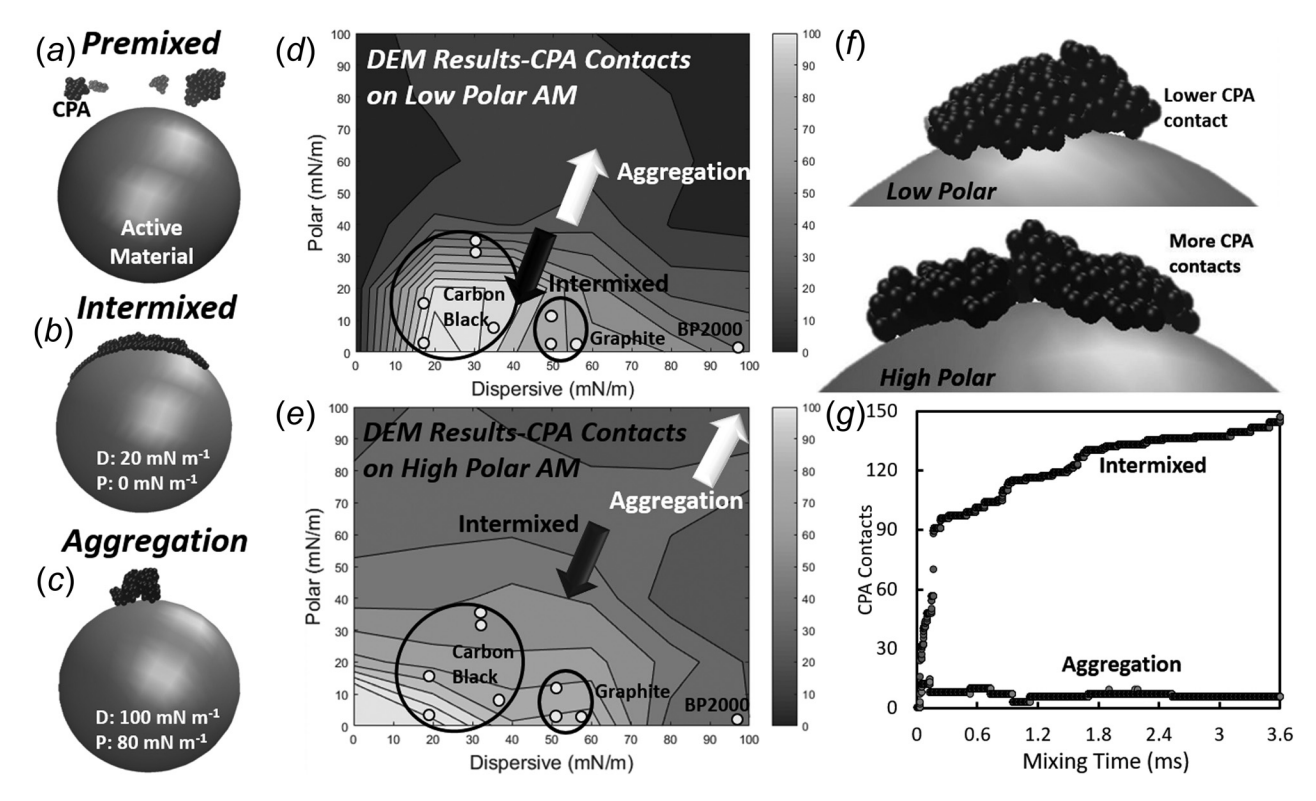


Fig. 4 AM-CPA mixing. DEM simulation snapshots of AM-CPA mixing showing (a) premixing, (b) intermixing, and (c) aggregation. (d) DEM contour plot showing the number of CPA in contact with the AM surface when the AM polar component is 2 mN m^{-1} . (e) DEM contour plot showing the number of CPA in contact with the AM surface when the AM polar component is 100 mN m^{-1} . (f) CPAs showing increased contact with higher polar surface energy AM as compared to low polar surface energy. (g) Comparison of mixing time found in DEM cases where intermixing and aggregation occurs.

component of the AM particle to 100 mN m⁻¹ while keeping the dispersive component to the same as before. This case was used to represent an AM material with a high polar surface energy component as shown in previous studies [12,22]. It is expected that DEM results will show higher CPA contact points as compared to Fig. 4(d) due to the higher interfacial energy between the AM and CPA surface. This expectation was confirmed by the plotting the CPA contact points (Fig. 4(e)) from the resulting DEM simulations where the AM had higher polar surface energy. The contour plot using a low polar component displayed a large 0-25 contact point area denoting aggregate formation; in the new contour plot using a larger polar component, this area is mostly replaced by 25-50 contact point areas. While these areas denote relatively few contact points when compared to the number of contacts associated with peak intermixing, it does signify the CPA agglomerate is attached to the AM and slowly conforming to the surface (Fig. 4(f)). The same CPA agglomerate from the 0-10 contact point area when the AM particle has a small polar surface energy component shows a lower degree of conformation (Fig. 4(f)).

The dots located on the DEM simulation contour plots (Figs. 4(d) and 4(f)) denote previously measured [21,31–36] surface energy values of carbon materials. They are used to show the expected mixing behavior of common carbon-based CPA materials. Surface energy measurements of graphite powders had a minimal polar component (0.54 mN m⁻¹) while the dispersive component was around 56.27 mN m⁻¹ [21,31]. Graphite surface energy measurements can be used to gain insight into the surface energy characteristics of carbon, but it may not be representative of the more commonly used CPA material (Carbon Black) due to its significantly larger size ($\sim 10 \, \mu m$). Previous studies [32–34] measuring Carbon Black surface energy show a similar low polar component when compared to graphite, but the dispersive component is typically measured at smaller values in the range of

18–35 mN m $^{-1}$. An increase in the Carbon Black polar surface energy component can be achieved through surface modification by way of acid–base treatments as detailed by Park et al. [35] where the treatments can be used to obtain a polar surface energy component up to 33.1 mN m $^{-1}$ [36].

The rate of mixing between an intermixed and aggregated case can be studied from the resulting DEM outputs to gain insight into how the CPA agglomerate begins to change shape when interacting with the AM particle. Figure 4(g) shows that an intermixed case (where the dispersive and polar components were set to $20\,\mathrm{mN}~\mathrm{m}^{-1}$ and $10\,\mathrm{mN}~\mathrm{m}^{-1}$, respectively) quickly achieves 90 CPA contacts (of the 200 total) within $\sim\!0.2\,\mathrm{ms}$ and then the number of contacts steadily increased. An aggregated case (where the polar and dispersive components were set to $100\,\mathrm{mN}~\mathrm{m}^{-1}$) shows very few CPA contact points on the AM surface. This is due to the work of adhesion between the AM and CPA being large enough that some of the exposed CPA will stay in contact with the AM surface, but not large enough such that it overcomes the very high work of cohesion between the particles in the CPA agglomerate.

3.3 Binder Additive-Conductive Additive. The two previous cases dealt with the mixing behaviors of different additives among active material particles, but intermixing within the additives is also needed to ensure more efficient usage of the materials. Minimal intermixing within the additives will give way to lower bonding strength as the BPA will not create enough contacts with the CPA material. DEM simulations for the BPA-CPA mixing case were carried out with the surface energy components of the BPA set according to the measured PVDF surface energy values [21] while the surface energy components of the CPA were changed. According to a previous study [22] where analytical models are presented for predicting material mixing behavior

Journal of Micro- and Nano-Manufacturing

DECEMBER 2017, Vol. 5 / 040902-5

based on surface adhesion, the BPA and CPA are expected to intermix with each other when the dispersive and polar surface energy components are between 10 and 40 mN $\rm m^{-1}$ and 0 and $20\,\rm mN~m^{-1}$, respectively. Outside of this region, it is more likely that the CPAs and BPAs will exhibit minimal interaction with each other.

Discrete element method simulations were used to check this expectation with $0.5 \,\mu m$ spheres representing BPA (20 total) and $0.25 \,\mu\mathrm{m}$ spheres representing CPA (400 total). The surface energy components of CPA were set to 20 mN m⁻¹ and 10 mN m⁻² respectively. These values were selected as they are the values associated with peak intermixing based on the previously presented analytical model [22]. If the model is correct, then the DEM simulation should show a high degree of BPA and CPA intermixing. In the simulation, it was found that individual BPA were embedded within an agglomerate of CPA (Fig. 5(a)). An enhanced view more readily shows this behavior where a monolayer of CPA is formed around BPA. Another simulation was used to confirm the opposite case where BPA and CPA should not intermix as well, forming an aggregate. For this simulation, both the dispersive and polar surface energy components for CPA were set to $100 \,\mathrm{mN} \,\mathrm{m}^{-1}$. The results of this case confirm the predicted mixing behavior where CPA form a large agglomerate (Fig. 5(b)) with BPA only attached to the surface of the CPA agglomerate. Unlike the intermixed case where individual BPA are surrounded by CPA, the CPA in this case have a work of cohesion too large to enable the BPA to break apart the attached CPA surfaces. Note that BPA only attach to the surface of CPA agglomerate with embedding into CPA, which is clearly different from the intermixing case.

3.4 Active Material-Binder Additive-Conductive Additive.

The previous DEM mixing cases considered only mixing two materials, but in the actual case all three materials will need to be mixed together. Two DEM simulations were considered to represent cases of Li-ion battery electrode material mixing. A single AM particle $10\,\mu\text{m}$ particle was mixed among $0.5\,\mu\text{m}$ particles representing the BPA (20 total) and $0.25\,\mu\text{m}$ particles representing the CPA (400 total). For both DEM simulations, the surface energy for the BPA was based on the previously discussed PVDF results and the surface energy for the CPA was set with the same values as the intermixed case from Sec. 3.3 (dispersive and polar surface energy components were $20\,\text{mN}$ m⁻¹ and $10\,\text{mN}$ m⁻¹, respectively). The surface energy values of CPA are also representative of previous measurements of Carbon Black [32]. The first DEM simulation had the AM surface energy measurements based on low polar AM, representative of as-received LCO from a

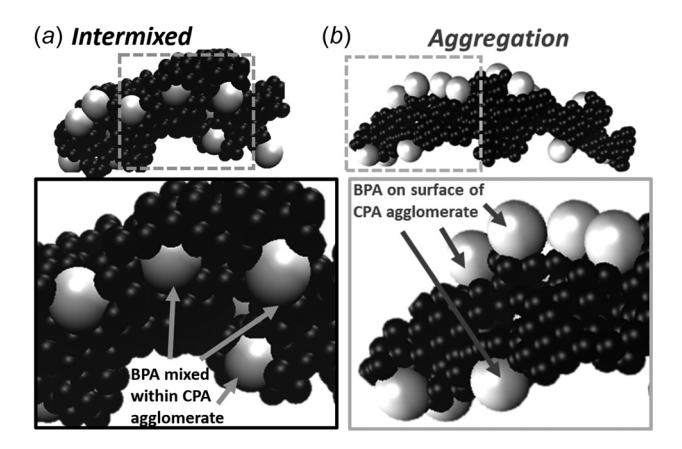


Fig. 5 BPA-CPA mixing: confirmation of analytical modeling results where a predicted intermixed case is confirmed by a DEM simulation (a) and where a predicted aggregation case is confirmed by another DEM simulation (b)

previous study [22]. Figure 6(a) shows the outcome of the DEM simulation where the BPA and CPA were dispersed on the AM surface. BPA is shown to be intermixed among the CPA particles with minimal agglomerations of BPA. For the other case, the polar surface energy component was increased to 100 mN m⁻¹ to represent higher polar AM measurements from previous studies [12,22]. The resulting DEM simulation shows similar results (Fig. 6(b)) to the previous case. BPA and CPA are dispersed on the AM surface while the BPA particles show no signs of aggregation. The behavior of the BPA on the two AM surfaces is expected based on the DEM simulation results when only AM and BPA are mixed as the two AM surface energies in this case lie within the area related to intermixing (Fig. 3(d)). For CPA, the DEM simulation results with only the AM and CPA are mixed largely predict that CPA will have more contact with the higher polarity AM surface than the low polar AM. In the case where all three material types are mixed, the CPA has a similar degree of contact regardless of the polarity of the AM material. However, it should be noted that the set CPA surface energy for these two cases show similar CPA contact with the AM surfaces when only the CPA and AM are mixed (the CPA surface energy used in this case lie within the 80-100 contact point area associated with high AM-CPA contact in both Figs. 4(d) and 4(e)). Using different CPA surface energy values could lead to different distributions of CPA on AM surfaces.

4 Experimental Verification

To verify the DEM results, Li-ion battery electrode materials were mixed and SEM micrographs were taken. For the case of AM-BPA mixing, as-received LCO powder was mixed with PVDF powder in a high-energy mixer. The contour plot developed from the DEM simulations point to intermixing occurring (Fig. 3(*d*)). An SEM micrograph of the mixed materials shows the expected intermixing behavior (Fig. 7(*a*)). A view of the DEM simulation using the same parameters shows (Fig. 7(*b*)) similar

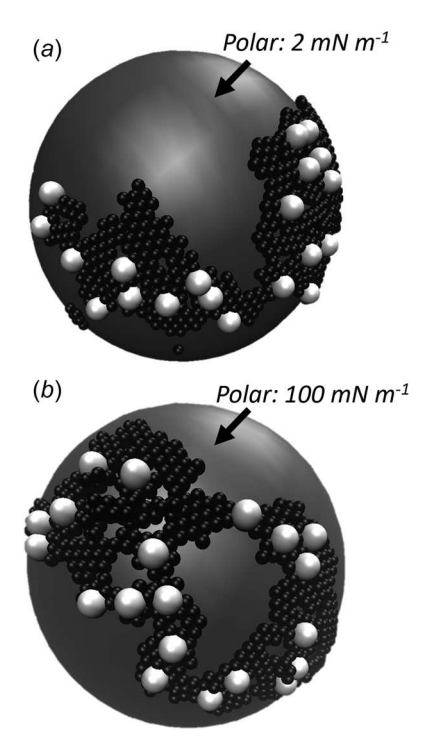


Fig. 6 AM-BPA-CPA mixing: (a) DEM simulation showing mixing behavior of all three materials when the AM polar surface energy is 2 mN m $^{-1}$ and (b) DEM simulation showing the mixing behavior of all three materials when the AM polar surface energy is increased to 100 mN m $^{-1}$

040902-6 / Vol. 5, DECEMBER 2017

Transactions of the ASME

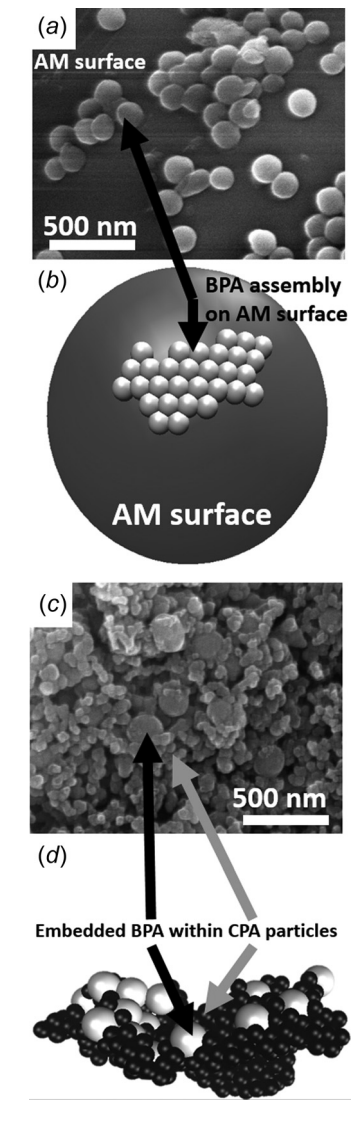


Fig. 7 Experimental mixing comparison: (a) SEM micrograph showing PVDF (representing BPA) particles attached to the surface of LCO (representing AM), (b) DEM confirmation of the experimental mixing result of AM-BPA with BPA particles attached to the AM surface, (c) SEM micrograph showing PVDF particles embedded within Super C65 carbon (representing CPA), and (d) DEM confirmation of the experimental mixing result of CPA-BPA with BPA particles embedded within the CPA

results where the BPA (PVDF) is attached to the AM (LCO). According to previous studies [22] where LCO was annealed to obtain a larger polar surface energy component, the mixing of annealed LCO with PVDF showed the BPA forming on the surface of the AM and intermixing. The DEM simulations in this study show similar behavior when the same surface energy components are used as the material properties.

For the case of AM-CPA mixing, a previous study [22] mixed LCO and Super C65 carbon with differing surface properties. It was found that annealed LCO, where the dispersive and polar surface energy components were 42.5 mN m^{-1} and $> 35.0 \text{ mN m}^{-1}$, respectively, contained more Super 65 carbon particles on the LCO surface when compared to as-received LCO where the dispersive and polar surface energy components were measured as 37.0 mN m⁻¹ and 1.35 mN m⁻¹, respectively. This behavior was confirmed by the DEM simulations (Fig. 4). It can be seen a large range of CPA surface energies has a higher degree of contact with the high polar AM surface (Fig. 4(e)) than with the low polar AM surface (Fig. 4(d)).

For BPA-CPA DEM comparisons, PVDF and Super C65 carbon were mixed in a high-energy mixer. SEM micrographs of the mixed powder (Fig. 7(c)) show individual PVDF particles embedded within the Super C65 particles.

A DEM simulation using similar surface energy properties of the materials shows similar intermixing behavior (Fig. 7(d)). The BPA particles exhibit minimal contact with one another as the BPA particles are individually embedded with the CPA particles.

5 Conclusion

In this paper, the effect particle surface energy had on the mixing characteristics of micro/nanosized Li-ion battery electrodes powders was studied. A DEM model based on the adhesive interactions of the Li-ion battery electrode particles was developed to simulate various mixing cases. DEM simulations were carried out using surface energy measurements assembled from previous studies and then compared with experimental mixing results. AM-BPA results show that only a small range of AM surface energy values will result in aggregation while AM-CPA mixing will be affected by different AM polar surface energy component values. BPA-CPA results show that BPA will be intermixed among CPA particles when the CPA surface energy values represent common values found in literature. For cases where all three material types are mixed (as is the case in production), the DEM simulations could accurately predict the mixing behavior of the accompanying experimental studies. This study shows that mixing behavior of other Li-ion battery electrode materials can be estimated when the surface energy component values are known.

Funding Data

- Division of Civil, Mechanical and Manufacturing Innovation (Grant No. 1462321).
- National Science Foundation (Grant Nos. CMMI-1462343 and CMMI-1462321).
- Intelligent System Center (ISC).
- Material Research Center (MRC) at Missouri University of Science and Technology.

References

- [1] Kraytsberg, A., and Ein-Eli, Y., 2016, "Conveying Advanced Li-Ion Battery Materials Into Practice The Impact of Electrode Slurry Preparation Skills, Adv. Energy Mat., 6(21), pp. 1–23
- [2] Lee, G.-W., Ryu, J.-H., Han, W., Ahn, K. H., and Oh, S. M., 2010, "Effect of Slurry Preparation Process on Electrochemical Performances of LiCoO2," J. Power Sources, 195(18), pp. 6049–6054.
- [3] Liu, D., Chen, L.-C., Liu, T.-J., Fan, T., Tsou, E.-Y., and Tiu, C., 2014, "An Effective Mixing for Lithium Ion Battery Slurries," Adv. Chem. Eng. Sci., 4(04), pp. 515-528.
- [4] Cetinkaya, T., Akbulut, A., Guler, M. O., and Akbulut, H., 2014, "A Different Method for Producing a Flexible LiMn₂O₄/MWCNT," J. Appl. Electrochem., **44**(2), pp. 209–214.
- Wei, Z., Xue, L., Nie, F., Sheng, J., Shi, Q., and Zhao, X., 2014, "Study of Sulfonated Polyether Ether Ketone With Pendant Lithiated Fluorinated Groups as Ion Conductive Binder in Lithium-Ion Batteries," J. Power Sources, 256, pp. 28–31.

 [6] Guerfi, A., Kaneko, M., Petitclerc, M., Mori, M., and Zaghib, K., 2007, "LiFePO₄ Water-Soluble Binder Electrode for Li-Ion Batteries," J. Power Sources, 250 pp. 28–31.
- ces, 163(2), pp. 1047-1052.
- [7] Spreafico, M. A., Cojocaru, P., Magagnin, L., Triulzi, F., and Apostolo, M., 2014, "PVDF Latex as a Binder for Positive Electrodes in Lithium-Ion Batteries," Ind. Eng. Chem. Res., **53**(22), pp. 9094–9100.
- [8] Daniel, C., 2008, "Materials and Processing for Lithium-Ion Batteries," JOM, 60(9), pp. 43-48.
- [9] Doberdo, I., Loffler, N., Laszczynski, N., Cericola, D., Penazzi, N., Bodoardo, S., Kim, G.-T., and Passerini, S., 2014, "Enabling Aqueous Binders for Lithium Battery Cathodes-Carbon Coating of Aluminum Current Collector," J. Power Sources, 248, pp. 1000-1006.
- [10] Li, J., Armstrong, B. L., Kiggans, J., Daniel, C., and Wood, D. L., 2012, "Optimization of LiFePO4 Nanoparticle Suspensions With Polyethyleneimine for Aqueous Processing," Langmuir, 28(8), pp. 3783-3790.
- [11] Bitsch, B., Dittmann, J., Schmitt, M., Scharfer, P., Schabel, W., and Willenbacher, N., 2014, "A Novel Slurry Concept for the Fabrication of Lithium-Ion Battery Electrodes With Beneficial Properties," J. Power Sources, 265, pp.

DECEMBER 2017, Vol. 5 / 040902-7

- [12] Li, J., Rulison, C., Kiggans, J., Daniel, C., and Wood, D. L., 2012, "Superior Performance of LiFePO₄ Aqueous Dispersions Via Corona Treatment and Surface Energy Optimization," J. Electrochem. Soc., 159(8), pp. A1152–A1157.
- [13] Li, C.-C., and Wang, Y.-W., 2013, "Importance of Binder Composition to the Dispersion and Electrochemical Properties of Water-Based LiCoO₂ Cathodes," J. Power Sources, 227, pp. 204–210.
- [14] Du, Z., Rollag, K. M., Li, J., An, S. J., Wood, M., Sheng, Y., Mukherjee, P. P., Daniel, C., and Wood, D. L., 2017, "Enabling Aqueous Processing for Crack-Free Thick Electrodes," J. Power Sources, 354, pp. 200–206.
- [15] Loeffler, N., von Zamory, J., Laszczynski, N., Doberdo, I., Kim, G.-T., and Passerini, S., 2014, "Performance of LiNi_{1/3}Mn_{1/3}Co_{1/3}O₂/Graphite Batteries Based on Aqueous Binder," J. Power Sources, 248, pp. 915–922.
- [16] Koike, S., and Tatsumi, K., 2007, "Preparation and Performances of Highly Porous Layered LiCoO₂ Films for Lithium Batteries," J. Power Sources, 174(2), pp. 976–980.
- [17] Kuwata, N., Kawamura, J., Toribami, K., Hattori, T., and Sata, N., 2004, "Thin-Film Lithium-Ion Battery With Amorphous Solid Electrolyte Fabricated by Pulsed Laser Deposition," Electrochem. Commun., 6(4), pp. 417–421.
- [18] Yan, B., Liu, J., Song, B., Xiao, P., and Lu, L., 2013, "Li-Rich Thin Film Cathode Prepared by Pulsed Laser Deposition," Sci. Rep., 3, pp. 1–5.
- [19] Baggetto, L., Unocic, R. R., Dudney, N. J., and Veith, G. M., 2012, "Fabrication and Characterization of Li-Mn-Ni-O Sputtered Thin Film High Voltage Cathodes for Li-Ion Batteries," J. Power Sources, 211, pp. 108–118.
- [20] Chiu, K.-F., 2007, "Lithium Cobalt Oxide Thin Films Deposited at Low Temperature by Ionized Magnetron Sputtering," Thin Solid Films, 515(11), pp. 4614–4618.
- [21] Ludwig, B., Zheng, Z., Shou, W., Wang, Y., and Pan, H., 2016, "Solvent-Free Manufacturing of Electrodes for Lithium-Ion Batteries," Sci. Rep., 6, pp. 1–10.
- [22] Ludwig, B., Liu, J., Chen, I.-M., Liu, Y., Shou, W., Wang, Y., and Pan, H., 2017, "Understanding Interfacial-Energy-Driven Dry Powder Mixing for Solvent-Free Additive Manufacturing of Li-Ion Battery Electrodes," Adv. Mater. Interfaces, epub.
- [23] Li., S., Marshall, J. S., Liu, G., and Yao, Q., 2011, "Adhesive Particulate Flow: The Discrete-Element Method and Its Application in Energy and Environmental Engineering," Prog. Energy Combust. Sci., 37(6), pp. 633–668.

- [24] Deng, X., Scicolone, J. V., and Dave, R. N., 2013, "Discrete Element Method Simulation of Cohesive Particles Mixing Under Magnetically Assisted Impaction," Powder Technol., 243, pp. 96–109.
- [25] Chokshi, A., Tielens, A. G. G. M., and Hollenbach, D., 1993, "Dust Coagulation," Astrophys. J., 407(2), pp. 806–819.
- [26] Johnson, K. L., Kendall, K., and Roberts, A. D., 1971, "Surface Energy and the Contact of Elastic Solids," Proc. R. Soc. London A, 324(1558), pp. 301–313.
- [27] Fowkes, F. M., 1968, "Calculation of Work of Adhesion by Pair Potential Summation," J. Colloid Interface Sci., 28(3-4), pp. 493-505.
- [28] Tsuji, Y., Tanaka, T., and Ishida, T., 1992, "Lagrangian Numerical Simulation of Plug Flow of Cohesionless Particles in a Horizontal Pipe," Powder Technol., 71(3), pp. 239–250.
- [29] Wu, S., 1971, "Calculation of Interfacial Tension in Polymer Systems," J. Polym. Sci. C, 34(1), pp. 19–30.
- [30] Morra, M., Occhiello, E., Marola, R., Garbassi, F., Humphrey, P., and Johnson, D., 1990, "On the Aging of Oxygen Plasma-Treated Polydimethylsiloxane Surfaces," J. Colloid Interface Sci., 137(1), pp. 11–24.
- [31] Lee, J., and Lee, B., 2017, "A Simple Method to Determine the Surface Energy of Graphite," Carbon Lett., 21(1), pp. 107–110.
- [32] Mezgebe, M., Shen, Q., Zhang, J.-Y., and Zhao, Y.-W., 2012, "Liquid Adsorption Behavior and Surface Properties of Carbon Black," Colloids Surf. A, 403, pp. 25–28.
- [33] Wang, H. F., Troxler, T., Yeh, A. G., and Dai, H. L., 2007, "Adsorption at a Carbon Black Microparticle Surface in Aqueous Colloids Probed by Optical Second-Harmonic Generation," J. Phys. Chem. C, 111(25), pp. 8708–8715.
- [34] Siebold, A., Walliser, A., Nardin, M., Oppliger, M., and Schultz, J., 1997, "Capillary Rise for Thermodynamic Characterization of Solid Particle Surface," J. Colloid Interface Sci., 186(1), pp. 60–70.
- [35] Park, S.-J., Seo, M.-K., and Nah, C., 2005, "Influence of Surface Characteristics of Carbon Blacks on Cure and Mechanical Behaviors of Rubber Matrix Compoundings," J. Colloid Interface Sci., 291(1), pp. 229–235.
- [36] Arico, A. S., Antonucci, V., Minutoly, M., and Giordano, N., 1989, "The Influence of Functional Groups on the Surface Acid-Base Characteristics of Carbon Blacks," Carbon, 27(3), pp. 337–347.